

Clinical-Inspired Cytological Whole Slide Image Screening with Just Slide-Level Labels

Beidi Zhao, Wenlong Deng, Zi Han (Henry) Li, Chen Zhou, Zuhua Gao,
Gang Wang and Xiaoxiao Li, *Member, IEEE*

Abstract—Cytology test is effective, non-invasive, convenient, and inexpensive for clinical cancer screening. ThinPrep, a commonly used liquid-based specimen, can be scanned to generate digital whole slide images (WSIs) for cytology testing. However, WSIs classification with gigapixel resolutions is highly resource-intensive, posing significant challenges for automated medical image analysis. In order to circumvent this computational impasse, existing methods emphasize learning features at the cell or patch level, typically requiring labor-intensive and detailed manual annotations, such as labels at the cell or patch level. Here we propose a novel automated Label-Efficient WSI Screening method, dubbed LESS, for cytology-based diagnosis with only slide-level labels. Firstly, in order to achieve label efficiency, we suggest employing variational positive-unlabeled (VPU) learning, enhancing patch-level feature learning using WSI-level labels. Subsequently, guided by the clinical approach of scrutinizing WSIs at varying fields of view and scales, we employ a cross-attention vision transformer (CrossViT) to fuse multi-scale patch-level data and execute WSI-level classification. We validate the proposed label-efficient method on a urine cytology WSI dataset encompassing 130 samples (13,000 patches) and FNAC 2019 dataset with 212 samples (21,200 patches). The experiment shows that the proposed LESS reaches 84.79%, 85.43%, 91.79% and 78.30% on a urine cytology WSI dataset, and 96.53%, 96.37%, 99.31%, 94.95% on FNAC 2019 dataset in terms of accuracy, AUC, sensitivity and specificity. It outperforms state-of-the-art methods and realizes automatic cytology-based bladder cancer screening.

Index Terms—Computational Pathology, Whole Slide Image, Positive-unlabeled Learning, CrossViT.

I. INTRODUCTION

Cytology is a branch of pathology commonly used for cancer screening and early diagnosis in many parts of the body,

Manuscript submitted 22 May 2023. This work is supported in part by the Natural Sciences and Engineering Research Council of Canada (NSERC), NVIDIA Hardware Award, Compute Canada and Health Innovation Funding Investment (HIFI) Awards from the University of British Columbia.

B. Zhao, W. Deng, X. Li are with Department of Electrical and Computer Engineering, the University of British Columbia, Vancouver, BC V6T 1Z4 Canada (email: beidiz@ece.ubc.ca; dwenlong@ece.ubc.ca; xiaoxiao.li@ece.ubc.ca).

Zi Han (Henry) Li is with BC Cancer Agency, Vancouver, BC V5Z 4E6 Canada (email: henry.li@bccancer.bc.ca).

C. Zhou, Z. Gao, G. Wang are with BC Cancer Agency, Vancouver, BC V5Z 4E6 Canada and Department of Pathology, and Laboratory Medicine, the University of British Columbia, Vancouver, BC V6T 2B5 Canada (email: czhou@bccancer.bc.ca; zuhua.gao@ubc.ca; gang.wang1@bccancer.bc.ca).

including bladder [1], [2], cervix [3]–[5], breast [6], lung [7] and gastric [8] that analyzes cellular morphology and compositions [9], [10]. In cervical cancer screening, for example, cells are collected from the cervix and examined for abnormalities using a microscope. The examination can help detect pre-cancerous changes or early-stage cancer, allowing for prompt treatment and better outcomes. Compared to histopathology, cytology emphasizes the pathological characteristics of individual cells in a liquid base rather than histopathological slides with cells arranged in a specific architecture. Cytological and histopathological WSIs differ notably in their image properties, with the random cell distribution in cytological WSIs and potential artifacts, making the analysis of cytological WSIs more challenging compared to that of the more detailed and structured histopathological WSIs.

Diagnostics of cytological specimens in clinical cytology require formal training and evaluation by international organizations [11], and cytologists can find it very time-consuming and tedious to examine tens of thousands of cells under a microscope or using gigapixel whole slide images (WSIs) for malignancy [12], [13]. There is a growing demand for automated cytological WSI screening systems that offer high performance and enhance screening efficiency.

In recent years, machine learning technology has enabled feasible solutions for cytological WSI analyzing in various types of cancers. WSIs are in super high-resolution, which can be up to $10,000 \times 10,000$ pixels, thus data-driven methods on WSIs are computational costly. Traditional machine learning-based methods generally focus on cell detection [14], segmentation and classification [15].

Deep learning (DL) facilitates advanced pattern recognition, thereby becoming a trending strategy for cancer screening with cytological WSIs. Predominantly, current DL-based solutions adopt a two-stage approach. This includes a feature encoder operating at the patch or cell level, followed by a model for aggregating WSI information. As a result, existing methods typically require auxiliary fine-grained annotations to learn cell or patch-level feature embedding in the first stage, which are effort-consuming for cytologists [11] and can be noisy [16]. Moreover, annotations are typically disease or organ-specific, thus the algorithm cannot be generalized [17]. Efforts have been explored to reduce the lable efforts by using pretrained model or assigning slide labels as patch labels. Pretrained feature extractor models in cytological image screening [18]–[20] have become increasingly popular in recent years due to their

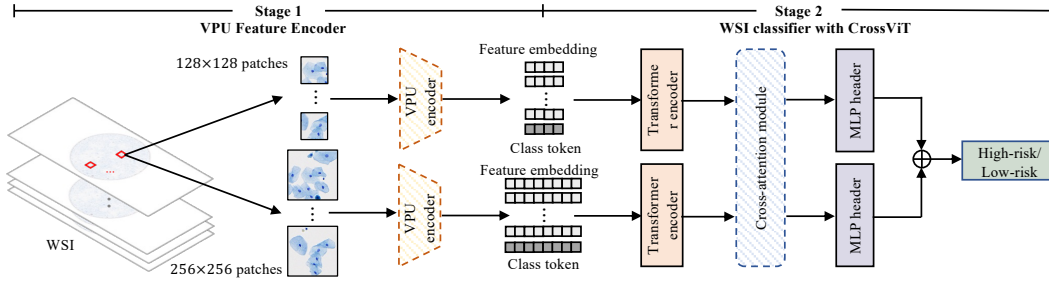


Fig. 1: Overview of LESS (a) Stage 1: WSI are cropped to patches of two sizes, and VPU feature encoders are trained to get the patch feature embedding (b) Stage 2: Information of different scales are exchanged in the cross-attention module, and the model gives prediction based on the fused information.

ability to extract high-level features from images efficiently. These models are typically trained on large datasets, such as ImageNet [21], using deep neural networks, and can be fine-tuned for specific tasks, such as cytological image analysis. However, such a strategy suffers from dropped performance due to domain gap due to the distribution misalignment between ImageNet (or other pretrained data) and the the WSIs to be analyzed. Alternatively, slides labels were used as pseudo labels for patches in an attempt to perform fully-supervised learning using the pseudo label [22]. Obviously, the patch labels can be noisy particularly for malignant slides that can take normal patches as well. We validated the unsatisfactory of these two approaches in Table II(b).

To reduce labeling cost while with better performance guarantee, we aim to develop a novel and generalizable cytology WSI screening method with just slide-level labels. Our design is motivated by the following two clinical insights that were previously overlooked. Firstly, to better utilize slide-level labels, we leverage the intrinsic feature of cytology cases: malignant slides contain benign and suspicious lesion cells, whereas benign slides only include benign cells. Secondly, we consider inputs of multiple fields of view (FoV) following the clinical workflow that doctors often change the microscope scales to comprehensively assess individual cells and cells around them to ensure they make the correct diagnosis. Like the previous methods, we use a two-stage pipeline by learning patch embedding first and then aggregating it to WSI-level prediction. Two fundamental designs need to be reconsidered to harness the above clinical insights: (1) *How to learn reliable patch embedding with just slide-level labels?* (2) *How to empower our method by mimicking clinical screening?*

To this end, we propose **Label-Efficient WSI Screening** method, named **LESS**, for cytology-based diagnosis. The framework is depicted in Fig. 1. The first stage is to learn the feature embedding of benign and malignant patches with only WSI-label using a weakly-supervised variational positive-unlabelled (VPU) learning model [22]. The second stage uses a cross-attention-based Vision Transformer (CrossViT) [23] to conduct WSI screening by capturing and interacting information from multiple scales with different FoV. The contributions of this paper are summarized as follows:

- We propose a DL-based automatic WSI screening model training without having to resort to specialists for specific

manual annotations. Our method, **LESS**, achieves high performance on two datasets with just slide-level labels;

- We adopt a weakly-supervised variational positive-unlabelled learning method that automatically learns the domain distributions of benign and malignant patches with only WSI-level labels, which can be generalized to different cytology WSIs;
- We apply the cross-attention module incorporating and exchanging patch information from multiple FoV to mimic clinical diagnosis.

II. RELATED WORK

A. Positive-Unlabeled Learning and Applications

Conventionally, binary classification problem has positive labels and negative labels. Positive-Unlabeled (PU) Learning aims to learn a binary classifier only from part of the positive data and unlabeled (PU) data that contains the other positive and negative-labeled data. Most current PU learning methods [24]–[26] rely on the misclassification risk associated with supervised learning. However, such methods can be susceptible to inaccuracies in estimating class prior probabilities. Chen et al. [22] proposed a variational principle that enables the quantitative evaluation of modeling errors for Bayesian classifiers directly from available data, leading to a loss function that can be efficiently computed without the need for class prior estimation or any intermediate estimations. PU Learning has been applied to studies of medical image analysis and proved to be effective in revising incomplete annotations for chest X-rays images, histopathology images, vascular CT images, etc. [27]–[29]. However, due to the gigabyte property of WSIs, PU learning models cannot be train on WSIs all at once. This work propose to design a PU learning model at patch-level that can learn reliable patch feature representation with the help of WSI labels.

B. Cytological WSI Cancer Screening

Recent work has seen encouraging outcomes for evaluating and screening WSIs with deep learning techniques. Awan et al. [1] proposed a cell detection and classification model according to different kinds of annotated cells and graded urine cytology WSIs based on the count of atypical and malignant cells. Sanghvi et al. [2] used convolutional neural networks to

extract urothelial cells and cell cluster features, then combine them with WSI features to perform urine cytological WSI screening. Li et al. [8] introduced a mixed supervision learning method with sufficient WSI-level coarse annotations and a few pixel-level labels for effective gastric cytology WSI classification. Cao et al. [5] introduced the attention module to a feature pyramid network to screen cervical cancer with the help of cell abnormal probability from an AttFPN inference model. Zhang et al. [3] proposed a whole slide cervical cancer screening model by contrasting a graph attention network constructed by top-k and bottom-k suspicious patches. Cao et al. [5] incorporated an attention module into a feature pyramid network to extract multi-scaled features of convolutional neural networks. It validated the effectiveness of the attention mechanism from cell-level detection, patch-level classification, and case-level classification. Although methods mentioned above achieved inspiring results, they all need manually annotated cell or patch labels, which are laborious and disease-specific, that cannot be generalized to wider applications.

III. METHODOLOGY

This work aims to efficiently and effectively utilize slide-level labels to screen out high-risk cancer WSIs by incorporating information from multiple FoV without cell or patch-level annotations. In this section, we will describe the overall pipeline and introduce the key technical contributions and rationale of the design.

A. Overview of the Proposed Pipeline

As shown in Fig. 1, the overall pipeline of our proposed method LESS contains two stages, including 1) patch embedding learning and 2) multi-scale fusion learning.

We begin with cropping the WSI into patches following previous work [1]–[3], [5], [8] in the first stage. This stage is to learn effective feature embedding of patches so that the embedding of patches is integrated with the fusion stage to get the prediction over WSI. In contrast to previous studies that 1) rely on fine-grained labels which is costly, and 2) employ pretrained models or assign slide-level labels as patch-level labels which is not necessitate fine-grained labels but sacrifice performance. Our objective is to eliminate the requirement for supplementary labeling while concurrently obtaining a high performance of WSI classification. Nonetheless, this endeavor presents a substantial challenge: the extraction of fine-grained patch representations from rather coarse label information. To overcome this, we employ a weakly-supervised-learning strategy that solely leverages WSI-level labels. This is facilitated via Variational Positive-Unlabeled (VPU) learning, a mechanism capable of autonomously refining optimal labels to supervise representation learning. Thus we will first introduce the critical novel VPU-based patch feature encoder to efficiently learn feature representation of benign and malignant patches with only patient labels (see Sec. III-B). We begin from the problem setting of PU learning in Sec. III-B.1, then introduce the variational principle in Sec. III-B.2 and MixUp-based consistency regularization in Sec. III-B.3.

Despite learning effective features, the gigabyte-sized nature of WSIs still necessitates a model capable of integrating this extensive information. The challenge is to design a more effective fusion that mimics the clinical WSI screening. Therefore, we introduce a CrossViT-based multi-scale fusion method to incorporate and exchange information from different FoV in Sec. III-C. We will begin with Vision Transformer, which is the backbone of CrossViT in Sec. III-C.1, then introduce the structure of CrossViT (Sec. III-C.2) and the cross-attention module with the most essential attention-mechanism in Sec. III-C.3.

B. Variational Positive-Unlabeled Learning Encoder

1) *PU Learning*: PU learning is a binary classification problem with input from labeled positive dataset $\mathcal{P} = \{x_1, \dots, x_M\}$ and an unlabeled dataset $\mathcal{U} = \{x_{M+1}, \dots, x_{M+N}\}$, which contains true positive and negative samples. Assuming that labeled and unlabeled data are independently drawn as

$$\mathcal{P} = \{x_i\}_{i=1}^M \stackrel{\text{i.i.d}}{\sim} f_{\mathcal{P}}, \quad \mathcal{U} = \{x_i\}_{i=M+1}^{M+N} \stackrel{\text{i.i.d}}{\sim} f, \quad (1)$$

where f is the distribution of positive data, f is the distribution of unlabeled data. There is a set $\mathcal{X} \subset \mathbb{R}^d$ that satisfies $\int_{\mathcal{X}} f_{\mathcal{P}}(x) dx > 0$ and

$$\Phi^*(x) = 1, \quad \forall x \in \mathcal{X}. \quad (2)$$

The goal is to approximate an ideal Bayesian classifier

$$\Phi^*(x) \triangleq \mathbb{P}(y = +1 | x) \quad (3)$$

that can accurately predict true positive and negative input labels from \mathcal{P} and \mathcal{U} .

Based on the fact that both malignant and benign patches exist in malignant samples, whereas benign samples only contain benign patches, we introduce positive-unlabeled (PU) [22] learning to maximize the utilization of slide-level annotation. Specifically, the positive set \mathcal{P} is formed by image patches from benign slides, while the unlabeled set \mathcal{U} comprises patches from malignant slides. Then, the PU learning method trains a binary classifier on these sets to enable accurate prediction of the class labels of the patches in malignant slides.

Most PU learning methods [24]–[26], [30] require class-prior estimation, which is to estimate $\pi_{\mathcal{P}} = \mathbb{P}(y = +1)$, *i.e.*, the proportion of benign patches in all patches from malignant slides in our application. However, obtaining such information is unfeasible without fine-grained patch-level annotations. To overcome this challenge, we propose to use a variational positive-unlabeled learning model [22] as the feature encoder to learn patch-level features. This approach enables us to build an effective classifier for identifying benign and malignant patches with only WSI-level labels.

2) *VPU without Class Prior Estimation with Variational Principle*: The illustration of the variational principle is shown in Fig. 2(a). With the learned classifier Φ approximated to the ideal Bayesian classifier Φ^* , the variational principle is driven

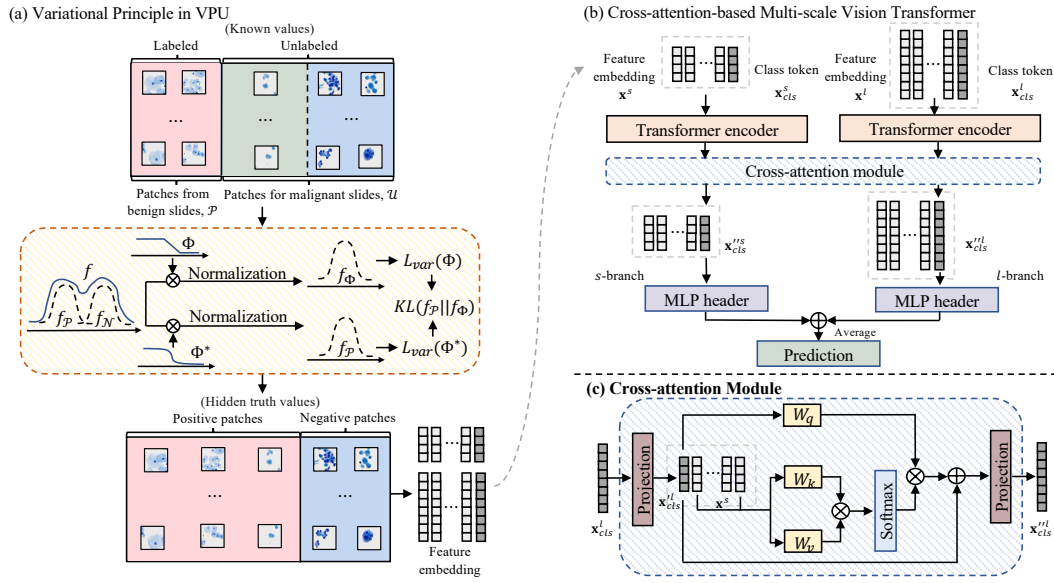


Fig. 2: Illustration of variational principle used in VPU and CrossViT structure with the cross-attention module. (a) VPU encoder aims to learn a Bayesian classifier from the dataset with only partial positive samples labeled. (b) Features of different scaled patches obtained by VPU are passed to CrossViT, which gives WSI-level predictions based on multi-scaled information. (c) Half of the inner structure of the cross-attention module. Class token of one branch acts as the query and interact information with embedding tokens from the other branch.

by the approximation that

$$\begin{aligned} f_{\mathcal{P}}(x) &= \frac{\mathbb{P}(y = +1 | x) \mathbb{P}(x)}{\int \mathbb{P}(y = +1 | x) \mathbb{P}(x) dx} \\ &\approx \frac{\Phi(x) f(x)}{\mathbb{E}_f[\Phi(x)]} \triangleq f_{\Phi}(x) \end{aligned} \quad (4)$$

with (3). Thus, we can minimize the KL divergence of learned positive distribution $f_{\mathcal{P}}$ and f_{Φ} . The KL divergence can be written as

$$KL(f_{\mathcal{P}} || f_{\Phi}) = L_{var}(\Phi) - L_{var}(\Phi^*), \quad (5)$$

where $L_{var}(\Phi)$ is the variational loss of the learned classifier, and $L_{var}(\Phi^*)$ is the variational loss of the ideal classifier. From [22], since $L_{var}(\Phi^*)$ is invariant, and KL-divergence is always non-negative, $L_{var}(\Phi)$ provides a variational upper bound of $L_{var}(\Phi^*)$. To minimize the KL divergence, we only need to minimize

$$L_{var}(\Phi) \triangleq \log \mathbb{E}_f[\Phi(x)] - \mathbb{E}_{f_{\mathcal{P}}}[\log \Phi(x)], \quad (6)$$

where f is the distribution of unlabeled data. As a result, The variational principle enables PU learning to learn the binary classifier without the class prior.

3) MixUp-Based Consistency Regularization: Due to the small size of labeled data, minimizing $\mathcal{L}_{var}(\Phi)$ with a complex Φ could result in overfitting and underestimation of Φ^* for the positive unlabeled data that is far from the positive labeled data. Following [23], a MixUp-based [31] consistency loss between labeled and unlabeled data is added to the variational loss 6 as a regularization term to the loss function to avoid overfitting,

$$\mathcal{L}_{reg}(\Phi) = \mathbb{E}_{\tilde{\Phi}, \tilde{x}} \left[\left(\log \tilde{\Phi} - \log \Phi(\tilde{x}) \right)^2 \right], \quad (7)$$

with

$$\begin{aligned} \gamma &\stackrel{\text{i.i.d}}{\sim} \text{Beta}(\alpha, \alpha), \\ \tilde{x} &= \gamma \cdot x^{\mathcal{P}} + (1 - \gamma) \cdot x^{\mathcal{U}}, \\ \tilde{\Phi} &= \gamma \cdot 1 + (1 - \gamma) \cdot \Phi(x^{\mathcal{U}}). \end{aligned}$$

α is the parameter of Beta distribution, \tilde{x} is a mixed sample generated by randomly selected sample $x^{\mathcal{P}}$ from the positive set and $x^{\mathcal{U}}$ from the unlabeled set, $\tilde{\Phi}$ is the guessed probability $\mathbb{P}(y = +1 | x = \tilde{x})$ generated from the linear interpolation of the true label and the prediction of model Φ . It is performed between labeled and unlabeled samples, adding smoothness to the model. Thus, the final objective function of the first stage is as follows

$$\min_{\Phi} \mathcal{L}(\Phi) = \mathcal{L}_{var}(\Phi) + \lambda \mathcal{L}_{reg}(\Phi), \quad (8)$$

where $\lambda \in [0, 1]$ is a parameter of the regularization term.

C. WSI Screening with CrossViT

Intuitively from cytologists examining slides under different magnifications for screening, we adopt a multi-scale cross-attention vision transformer (CrossViT) [23] that takes patches from different FoV to classify the whole slide images.

1) Vision Transformer: Fig. 2(b)(c) show a variant of ViT. Typically, ViT consists of three parts: (1) feature embedding layers; (2) transformer encoder blocks that include self-attention modules and (3) MLP header for classification. Embedding layers are used to project patches into tokens linearly. Like the original Transformer used in Natural Language Processing [32], a learnable class token (CLS) is added to the sequence (9). Then, all tokens are fed into the transformer encoder blocks with multi-head self-attention (MSA) modules.

For each self-attention module, it is combined with a two-layer multilayer perceptron constructed feed-forward network (FFN) with GELU [33] after the first linear layer and dropout (10). Between each transformer block, layer normalization is applied to reduce the effect of covariate shifts in the model. Next, CLS is regarded as the summarization of all tokens and passed to the MLP header to give the final prediction (11), (12). Suppose the input of ViT is \mathbf{x}_0 , the embedding of \mathbf{x}_0 after the k -th block is

$$\mathbf{x}_0 = [\mathbf{x}_{cls} \parallel \mathbf{x}_{patch}] + \mathbf{x}_{pos}, \quad (9)$$

$$\mathbf{x}'_k = \mathbf{x}_{k-1} + \text{MSA}(\text{LN}(\mathbf{x}_{k-1})), \quad k = 1 \dots K, \quad (10)$$

$$\mathbf{x}_k = \mathbf{x}'_k + \text{MLP}(\text{LN}(\mathbf{x}'_k)), \quad k = 1 \dots K, \quad (11)$$

$$\mathbf{y} = \text{LN}(\mathbf{x}_K^0), \quad (12)$$

where $\mathbf{x}_{cls} \in \mathbb{R}^{1 \times C}$ is the class token, $\mathbf{x}_{patch} \in \mathbb{R}^{N \times C}$ is the patch token, $\mathbf{x}_{pos} \in \mathbb{R}^{(1+N) \times C}$ is the position embedding, and \mathbf{y} is the output. N is the number of patch tokens and C is the number of dimension of the embedding. \mathbf{x}_K^0 is the class token after K blocks.

2) Multi-Scale Vision Transformer: The illustration of CrossViT [23] is shown in Fig. 2(b), including two branches of ViT with a cross-attention module between transformer encoders and MLP headers that incorporate and exchange information. In our work, the output of feature embedding layers in ViT is replaced by the feature embedding obtained from VPU with two input patch sizes. We delete the position embedding \mathbf{x}_{pos} since cells in cytological WSIs are uniformly distributed, and the position-agnostic property will not harm the result. To this end, we feed two-branch tokens \mathbf{x}^s and \mathbf{x}^l , where l means the branch of large patches and s means the branch of small patches, to the multi-scale transformer encoder, followed by a cross-attention module. Outputs are then passed through two MLP headers respectively, and the final prediction is obtained from the average score of classifiers. In this stage, we use cross-entropy between true slide-level labels and predicted labels as the loss function. The fundamental technique in CrossViT that enables multi-scale fusion is the *Cross-attention Module*, described in details below.

3) Cross-attention Module: The cross-attention module is a component used in various DL architectures, particularly in transformers, enables models to prioritize different parts of the input data at varying levels of granularity, efficiently capturing long-range dependencies, thereby enhancing interpretability and performance of the model. In our work, it consists of large-scale branch (l -branch) and small-scale branch (s -branch). Fig. 2(c) shows the l -branch, which exchanges information between the large-scale class token $\mathbf{x}_{cls}^l \in \mathbb{R}^{d_l}$ with d_l dimension and embedding tokens \mathbf{x}^s from the s -branch. The projection layer $f^l(\cdot)$, including a LayerNorm [34] followed by GELU [33] and a linear layer, is to make \mathbf{x}_{cls}^l align with \mathbf{x}^s in dimension

$$\mathbf{x}_{cls}^l = f^l(\mathbf{x}_{cls}^l) \in \mathbb{R}^{d_s}. \quad (13)$$

Then, \mathbf{x}_{cls}^l is concatenated with \mathbf{x}^s . The module conducts cross-attention (CA) between \mathbf{x}_{cls}^l and \mathbf{x}^s as

$$\mathbf{q} = \mathbf{x}_{cls}^l \mathbf{W}_q, \quad \mathbf{k} = [\mathbf{x}_{cls}^l \parallel \mathbf{x}^s] \mathbf{W}_k, \quad \mathbf{v} = [\mathbf{x}_{cls}^l \parallel \mathbf{x}^s] \mathbf{W}_v, \quad (14)$$

$$\mathbf{A}^l = \text{Attention}(\mathbf{q}, \mathbf{v}, \mathbf{k}) = \text{softmax}(\mathbf{q}\mathbf{k}^\top / \sqrt{d_s/n})\mathbf{v}, \quad (15)$$

where $\mathbf{q}, \mathbf{k}, \mathbf{v} \in \mathbb{R}^{\sqrt{d_s/n}}$ are query, key and value, d_s is the feature embedding dimension of the s -branch, n is the number of heads, and \mathbf{A}^l is the attention map of the l -branch. In CA, only \mathbf{x}_{cls}^l is used as the query, as it contains information of l -branch and realizes linear computational complexity. Furthermore, the feed-forward network (FFN) in the original ViT [35] is replaced by a residual connection [36] to reduce the number of parameters and preserve information from \mathbf{x}_{cls}^l . To this end, we get the class token \mathbf{x}_{cls}^l after acquiring the information from the small-scale branch, namely

$$\mathbf{x}_{cls}^l = g^l(f^l(\mathbf{x}_{cls}^l) + \text{MCA}(\text{LN}([f^l(\mathbf{x}_{cls}^l) \parallel \mathbf{x}^s]))) , \quad (16)$$

where $\mathbf{x}_{cls}^l \in \mathbb{R}^{d_l}$, which is then passed through the back-projection layer $g^l(\cdot)$ to recover to its original dimensionality and added back to l -branch embedding tokens to continue going through the MLP header and predicting. Then, the output of the cross-attention module can be written as

$$\mathbf{z}^l = [g^l(\mathbf{x}_{cls}^l) \parallel \mathbf{x}^l]. \quad (17)$$

The s -branch follows a symmetric process by exchanging notations of l and s in (13)-(17).

To sum up, the whole pipeline contains two modules, one is the VPU model, the other is Cross-attention-based multi-scale ViT. The VPU model takes patches and slide-level label as input and generates patch feature embedding, which is passed to the CrossViT as input and get predictions of WSIs.

IV. EXPERIMENT

A. Experimental Setup

1) Dataset: We conduct experiments on two cytological image datasets: a urine cytological WSI dataset collected by BC Cancer Agency and a public breast high-resolution image dataset to screen out high-risk slides. Examples of datasets used in this paper are shown in Fig. 3.

Urine Cytological WSI Dataset. We first evaluate LESS on a urine cytological WSI dataset that contains 130 urine cytology Thinprep pad specimens scanned on a MoticEasyScan Infinity instrument at 40 \times magnification. All samples were screened and diagnosed by experienced cytotechnologists, further confirmed by expert pathologists and approved by the ethics committee. The average size is around 60,000 \times 60,000. The dataset contains high-risk (with subtypes of suspicious (19) and malignant (41)) and low-risk (with subtypes of benign (42), atypical (28)) samples.

FNAC 2019 [18]. To validate the generalizability of cancer screening, we show experimental results apart from the urine cytological WSI dataset. Given the scarcity of publicly available WSI datasets, we apply our method to a high-resolution cytological image dataset FNAC 2019 [18] with 2,048 \times 1,536 breast cytological images. It appears to be one

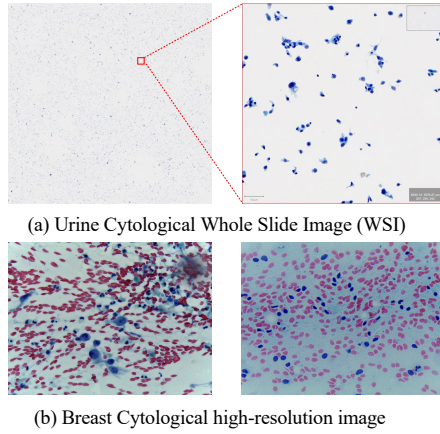


Fig. 3: Examples of the urine cytological WSI and breast cytological high-resolution images.

TABLE I: Hyperparameter setting of models. Model structures and hyperparameters are the same as those in the original papers if not listed. Learning rates are selected based on complexity of the model and stability of the training loss curve.

Hyperparameter Setting	Stage 1	Stage 2		
	VPU/PN	MLP	GNN/Fused GNN	ViT/CrossViT
Batch size	100	128		
Epochs	10	40		
Optimizer	Adam	Adam		
Learning rate (LR, initial, end)	$1e-4, 1.25e-5$	$1e-2, 5e-3$	$4e-4, 2e-4$	$1e-6, 5e-7$
Warmup ($\frac{1}{10}$ of the initial LR)	-	5 (with $\frac{1}{10}$ initial learning rate)		
LR scheduler	Step (0.5 every 2 epochs)	Cosine	Cosine	Cosine
Weight Decay	-	-	-	0
Drop	-	-	-	0.1
Drop path	-	-	-	0.1

of the few publicly available cytology datasets specified for classification models. The dataset consists of 212 fine-needle aspiration breast cell inspection images categorized benign (99) or malignant (113). Since our method is patch-based, they can be used comparable to WSIs.

2) Implement Details: We use sliding windows with 50% overlap to crop 128×128 patches [1]–[3], [5], [8] and design simple filters based on RGB pixel mean and standard deviation to screen out background and irrelevant information as shown in Fig. 4. The shown filters are for the urine cytological dataset, which can be customized and designed specific to a certain dataset. Then, we randomly keep 100 patches from each WSI and capture 256×256 patches from the WSI with the center of 128×128 patches for further analysis. If the number is less than 100, we use image augmentation methods to complete it. The backbone of the VPU feature encoder is a 7-layer CNN, with four convolutional layers and three linear layers. ReLU is used after each convolutional layer, and the final activation layer is LogSoftmax to get the predicted patch label. Feature embedding is extracted before the final linear layer. For the WSI screening model, the input are 384-dimension tokens from 128×128 patches and 768-dimension tokens from 256×256 patches. All experiments are implemented by PyTorch on the NVIDIA 3090Ti GPU.

We split training-testing randomly for five times to repeat the experiment. Benign and malignant WSIs are divided into 70% training data and 30% testing data to train the first-

stage model. The testing set for the second-stage consists of the testing set of the previous stage, plus all atypical and suspicious slides. As we have two stages, we train the first stage for 10 epochs and second-stage for 40 epochs with five random seeds for each split. Parameters of all models are shown in Table. I.

B. Performance Evaluation

1) Baselines: Since we are unable to directly compared with works with fine-grained annotations, for fair comparison, we consider the alternative method that directly uses slide-level label to supervise patch-level feature learning, different feature aggregation methods, single-scale strategies and unsupervised feature encoding methods. Table. II shows results of LESS and compared methods on the urine cytological WSI dataset, in which only results of 256×256 patches are shown since they contain information of 128×128 patches.

Comparison of Weakly-supervised Methods. We train a VGG16 used in previous work [37] by directly assigning WSI-label to the label of patches from WSIs to get the feature embedding before linear layer to compare with our VPU. VPU increases the performance of each second-stage feature aggregation method by over 1.99% accuracy and reduces the standard deviation. Here we define supervised learning of binary classification with pre-assigned positive and negative labels using cross entropy as positive-negative (PN) learning. Label noise can occur in PN learning when benign patches are incorrectly labeled malignant in high-risk WSIs. VPU encoder uses only confidently labeled benign patches for stable feature embedding, reducing the need for manual annotations and aiding WSI screening.

Comparison of Aggregation Strategies. We try different patch feature aggregation methods, including the estimated counting method [1] to deep-learning based multilayer perceptron (MLP), graph neural network (GNN) [and ViT [35]. RNN is not involved as [38] has shown the limitation of RNN-based aggregation. For the counting method, we set 50 as the high-risk threshold patch number for a WSI. For MLP, we use a pooling layer and a fully-connected layer. For GNN, we regard each patch as a node, patch feature embedding as node features, and connect nodes with cosine feature similarity > 0.9 , then train a graph convolutional network (GCN) [39]. Standard deviation of MLP and counting is larger than 10% for some metrics, which means they fluctuate enormously and are unreliable. The result shows that ViTs perform better than GNNs with features provided by VPU, reaching 83.36% accuracy. Unlike histopathology WSIs, cells in cytology WSIs are almost evenly distributed. Instead of referring to the structural relationship between cells, doctors may prefer to pay attention to the most critical cells in WSI screening.

Comparison of Multi-scale and Single-scale. We fuse multi-scale information with CrossViT and Fused GNN to compare with methods in the previous paragraph. For fused GNN, we follow [40] to concatenate the feature embedding of small and big patches and use the same graph construction method as the single-scale GNN. LESS is better than all single-scale-based methods by 1.50% accuracy, 1.34% AUC, while ensuring

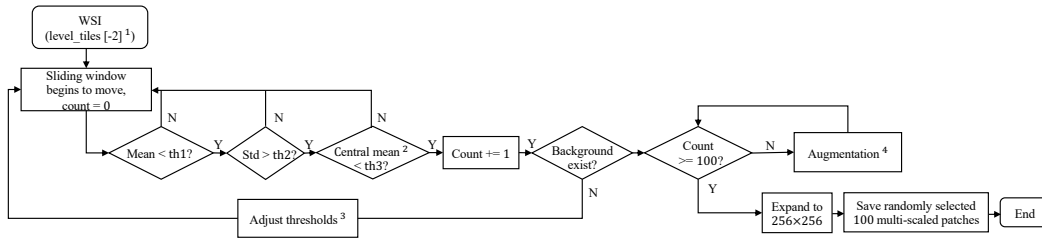


Fig. 4: Flowchart of WSI preprocessing. ¹ The level_tiles is generated from DeepZoomGenerator in python library Openslide; ² refers to the central $\frac{1}{2}$ area of the patch; ³ Thresholds should be designed based on the specific dataset. In our setting the initial thresholds are $th1 = 236$, $th2 = 10$, $th3 = 236$. $th1$ is used to screen out the background, $th2$ is used to screen out patches with large blank space and blurriness, $th3$ is used to ensure that cells are not only present at the border; ⁴ Data augmentation techniques used in our study include rotation, left-right flipping, top-bottom flipping, zooming.

TABLE II: Results (%) of WSI screening metrics for baselines and LESS on the urine cytological WSI dataset. For single-scale models, 256×256 patches are used as input. Mean and standard deviation are reported. Results in bold come from LESS.

(a) WSI-level screening with patch feature encoder that directly assigns WSI-label to patch-label and VPU.								
Method	PN				VPU			
	Acc	AUC	Sensitivity	Specificity	Acc	AUC	Sensitivity	Specificity
Counting	75.82(11.40)	75.39(7.74)	81.71(10.00)	76.06(11.09)	84.71(3.68)	72.91(4.99)	99.23(1.57)	59.54(4.60)
MLP	74.52(18.16)	74.25(18.45)	99.23(1.57)	85.54(20.70)	70.00(11.41)	70.09(11.97)	87.72(21.82)	67.56(15.08)
GNN	76.44(3.34)	76.02(3.59)	79.71(6.22)	76.03(2.29)	82.88(3.64)	84.09(3.41)	94.04(3.03)	74.22(4.40)
ViT	76.03(2.29)	75.76(2.33)	79.46(3.87)	72.72(4.24)	83.36(2.04)	83.67(2.44)	88.32(2.54)	78.19(2.44)
Fused GNN	80.55(3.03)	80.20(3.37)	83.01(5.52)	78.60(5.12)	83.29(1.50)	83.75(1.55)	89.28(2.81)	77.48(2.50)
CrossViT	78.56(2.49)	78.24(2.58)	81.29(3.81)	75.98(4.19)	84.79(2.13)	85.43(2.14)	91.79(3.19)	78.30(2.97)

(b) WSI-level screening with unsupervised learning feature encoding strategies.								
Method	Pretrained model on ImageNet				SimCLR (with 50 pretrain epochs)			
	Acc	AUC	Sensitivity	Specificity	Acc	AUC	Sensitivity	Specificity
GNN	74.59(1.04)	74.58(1.08)	79.05(1.81)	69.72(1.71)	79.67(1.78)	79.86(1.82)	84.55(3.20)	74.72(3.02)
ViT	74.65(2.45)	74.09(2.88)	80.65(5.12)	72.00(2.85)	80.36(4.52)	78.98(4.61)	78.25(3.93)	80.47(8.45)
Fused GNN	75.00(1.66)	74.79(1.70)	78.52(1.93)	70.86(2.24)	80.21(2.20)	79.79(2.52)	82.02(3.25)	77.98(1.62)
CrossViT	75.34(1.78)	75.99(1.88)	82.86(2.92)	72.41(2.41)	80.82(1.40)	80.53(1.45)	84.62(2.15)	77.78(2.61)

AUC over 85% and sensitivity over 90%, which are critical in clinical cancer screening. LESS also performs better than fused-GNN by over 0.6% on all metrics. It proves that we mimic the behaviour of medical experts looking at slides from different FoV during screening.

Comparison with Unsupervised Feature Encoder. Another strategy to learn the feature embeddings in stage one without additional fine-grained labels is via unsupervised learning. We compare the result of using a pretrained model to our model that trains from scratch. Also, we compare using the self-supervised SimCLR [41] as an alternative to our VPU feature encoder. Those two methods can be alternate choices for feature extraction in stage 1 of LESS. The result is shown in Table. II(b). The result of counting and MLP methods are omitted, as they are proved to be unreliable in Table. II(a). Parameters of SimCLR are kept the same as the original paper [42]. Here, SimCLR has already made WSI screening converge. From the table, we can observe that the result with the pretrained model on ImageNet is 3.22% lower than training from scratch in terms of accuracy, 2.25% lower in terms of AUC and 3.57% lower in terms of specificity. For the model with self-supervised SimCLR as feature encoder, accuracy, AUC, and sensitivity are worse than LESS by over 3.97%, and specificity is lower than LESS by 0.5%.

C. Interpretation and Explanation

To demonstrate the effectiveness of the cross-attention module, we leverage the attention score of its output class tokens to show patches with the highest attention scores. Although we perform binary classification, to have a better interpretation, we show that our model is explainable on four subtypes with the attention maps. We present two example WSIs per subtype from the testing data in Fig. 5. Small and big patches are with top-3 highest attention scores. Patches should contain information that can strongly support clinical judgment. Also, large and small patches should not overlap in content since we expect to get different information from multiple FoV.

First, we observe that the top patches of different resolutions from the same slide are not overlapped, indicating LESS effectively leverage complementary information from the multi-scale inputs. Second, the top attention slides reflect the critical clinical characteristics of each class, implying coincidence with the clinical diagnostic basis. Specifically, high-grade urothelial carcinoma is evident in Fig. 5(a), where numerous tumor cells demonstrate polymorphism, high N/C ratio, prominent nucleoli, irregular nuclei control and hypochromasia. Fig. 5(b) contains cells that are suspicious of high-grade urothelial carcinoma and a few normal intermediate urothelial cells. For suspicious cells, the N/C ratio increases, the chromatin has irregular hypochromasia, and the nuclear membrane exhibits marked irregularities. Fig. 5(c) shows cells



Fig. 5: 128×128 (left) and 256×256 (right) patches with top-3 attention scores are shown. Each block means a subtype of WSIs containing two examples, with the upper two blocks of high-risk and the lower two of low-risk. The row in the block means patches from the same WSI. The column means patches of the same size.

of two typical kinds of benign slides, including superficial benign urothelial cells and intermediate or parabasal urothelial cells. The former have frothy and abundant cytoplasm and pale, finely granular chromatin in the nuclei. The later have a similar size and characteristics as superficial cells but have less cytoplasm. Despite the high N/C ratio, they do not have other characteristics of urothelial carcinoma and are present in a neat honeycomb arrangement. Fig. 5(d) shows atypical urothelial cells with a high N/C ratio and an irregular nuclear contour. The absence of hyperchromasia and the presence of degenerated clumped chromatin preclude the diagnosis of suspicious or malignancy.

D. Ablation Study

We do ablation study experiment on the consistency regularization term in our objective function (8). We compare the result (shown in Table. III) of with and without the consistency regularization term to verify its effectiveness.

TABLE III: Results (%) of LESS with and without the consistency regularization term.

Ablation	Acc	AUC	Sensitivity	Specificity
W/o regularization	80.82 _(1.37)	81.21 _(1.64)	97.85 _(3.72)	75.32 _(3.70)
W/ regularization	84.79 _(2.13)	85.43 _(2.14)	91.79 _(3.19)	78.30 _(2.97)

E. Hyperparameter Sensitivity Analysis

In the existing PU learning works, the true label of the testing set is known, thus the true testing accuracy can be calculated. However, the ratio of benign and malignant patches is agnostic in the real world and will change with the number of randomly selected patches, so we use a posteriori approach

TABLE IV: Results (%) of WSI screening metrics for all baselines and LESS on FNAC 2019 dataset. Mean and standard deviation are reported. Results in bold come from LESS.

Method	FNAC			
	Acc	AUC	Sensitivity	Specificity
VPU + GNN	95.63 _(2.04)	92.36 _(4.09)	100.00 _(0.00)	94.24 _(2.35)
VPU + ViT	95.00 _(2.04)	94.67 _(2.17)	100.00 _(0.00)	91.49 _(3.17)
VPU + Fused GNN	95.98 _(1.77)	94.97 _(1.56)	98.75 _(2.80)	94.97 _(1.84)
LESS	96.53 _(0.86)	96.37 _(0.66)	99.31 _(1.54)	94.95 _(2.10)

to decide when to stop our VPU model according to the WSI screening result. Additionally, CrossViT has multiple structures based on various embedding token dimensions and numbers of heads, including tiny (96 and 192), small (192 and 384) and base (384 and 768) models [23]. We experiment on different ViT structures By extracting features of different dimensions.

Analysis of VPU Stopping Epoch. The number of VPU training epochs is a hyperparameter of LESS, which may affect the embedding results. In Fig. 6(a), the result shows that the WSI classification result is not sensitive to the epoch number of VPU, meaning it is robust to choose a wide range of stopping epoches for VPU to generate feature embedding.

Analysis of VPU Feature Dimension. We compare the feature embedding dimensions of VPU in Fig. 6(b). With the number of features increasing, the accuracy of WSI screening rises from 82.47% to 84.79% and then decreases to 83.22%. Also, higher embedding dimensions require more computational resources and training time, which may not be practical for clinical setups. In our implementation, we set epoch as 10, an earlier point, to save time and computing costs.

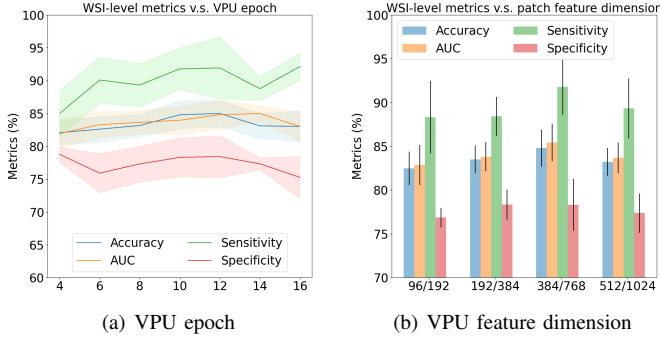


Fig. 6: Hyperparameter sensitivity analysis on VPU epoch and embedding dimension

F. Results on Public Dataset

We choose to conduct experiments on FNAC 2019 [18], a publicly available dataset with high-resolution breast cytological images truncated from whole slides, to validate the generalizability of LESS. It demonstrates that our method can be flexibly applied to different sized cytological images and across cancers. By testing the model on a diverse set of images from the public dataset, we are able to evaluate its generalization ability and assess its performance in a broader range of image features. The result of LESS on the FNAC dataset compared to baselines is shown in Table. IV. LESS for breast cancer screening shows promising results compared to baselines. For accuracy, our model reaches 96.53%, which is higher than that of baselines by over 0.55%. LESS also outperforms baselines by over 1.40% regarding AUC, achieving 96.37%. Meanwhile, our model is 99.31% for sensitivity and 94.95% for specificity, comparable to baselines. These results demonstrate our model is highly accurate and specific in detecting abnormalities in a wide range of cytological images, showing our proposed model LESS has the potential to improve diagnostic accuracy and efficiency in general clinical scenes.

V. DISCUSSION

In this work, we develop a DL framework which addresses the challenges of reliable patch feature learning and mimicking clinical screening from multi-scales. Specifically, we utilize a VPU feature encoder to learn patch feature embedding with just slide-level labels. Additionally, the model mimics the clinical screening process, incorporating CrossViT architecture with the cross-attention-based mechanism to incorporate comprehensive information from different FoV.

Cytological v.s. Histopathological WSIs. Cytological and histopathological WSIs have similar characteristics in size, digital methods, magnification, *etc.* Still, analyzing them are different from many aspects. First, cytology focuses on examining the quality and quantity of individual cells, it can be used for early and rapid screening and diagnosis of cancer or other diseases, whereas histopathology focuses on more detailed analysis of tissues and organs. Cells in cytological WSIs are at a random distribution and more prone to artifacts, distortion and cell overlapping, whereas cells in histopathological WSIs

provides a more accurate representation of tissue architectures. Therefore, methods for histopathological WSIs cannot be directly applied to cytological WSIs. Besides, annotation of cytology WSIs is more time consuming than that of histology WSIs, marking the need to get rid of annotations.

Contributions. One of the main contributions of our work is eliminating the dependence on fine-grained annotations, which saves time and labor, and can be generalizable to various cancers screening. Without specific fine-grained annotations, the model can capture features that was not previously described or recognized, which enables us to refine feature representation with just slide-level labels. Benefit from this property, our approach is flexible and generalizable across different diseases, not restricted to recognizing or segmenting specific cells used in previous work [1]–[3], [5], [8]. It can also be easily trained when fed with additional large number of samples in the future with no need of cell or patch-level annotations. Besides, we mimic the clinical diagnosing process to incorporate features from multiple FoV when examining the risk of a sample. Multi-scale features extracted from different neural network layers can capture local and global information about an object. Inspired by clinical diagnosis, our work is able to capture fine-grained details and larger-scale structures of patches and WSIs to learn more comprehensive features and make more confident decisions. Furthermore, we develop a method that adopts weakly-supervised learning with just slide-level label, which is better than unsupervised methods like using pretrained model as feature encoder or SimCLR. Training a model from scratch can help prevent overfitting and achieve better generalization performance. At the same time, LESS provides an indirect supervision through VPU learning, outperforming unsupervised methods which lack of guidance.

Limitation of PU Learning. The problem of PU learning is centered around training a classifier using data that comprises positive and unlabeled examples. The binary classification nature restricts the extension to multi-class datasets. Our dataset can be categorized into two classes, which are low-risk and high-risk. Nonetheless, if a more refined classification of WSIs is desired, such as categorizing them into benign, atypical, suspicious, and malignant groups, Multi-Positive and Unlabeled learning (MPU) is a possible solution. A solution for the MPU issue is provided in [43]. It involves learning from labeled data that comes from multiple positive classes and unlabeled data that are either from the positive classes or an unknown negative class by learning a discriminant function $F : \mathcal{X} \times \mathcal{Z} \rightarrow \mathbb{R}$ over the input and the encoded output pairs $(\mathbf{x}_1, \mathbf{z}_1), \dots, (\mathbf{x}_n, \mathbf{z}_n) \in \mathcal{X} \times \mathcal{Z}$. It generates the new output space \mathcal{Z} by encoding the original output space \mathcal{Y} . However, like most work before VPU [22], it requires estimating the class prior by [44], which may be challenging to obtain from patches without fine-grained annotations. Therefore, designing an MPU method that does not need class prior and can be applied to learn multi-class WSI patch feature representation is an open question and a promising future work.

VI. CONCLUSION

This paper proposes a novel label-efficient WSI screening model to learn reliable patch features and mimic clinical

screening from FoV. It completely eliminates the need for any fine-grained annotations. It saves manpower and time for annotation and can be extended to more applications of WSI screening, which provides a clinical solution with great value.

REFERENCES

- [1] R. Awan *et al.*, "Deep learning based digital cell profiles for risk stratification of urine cytology images," *Cytometry Part A*, vol. 99, no. 7, pp. 732–742, 2021.
- [2] A. Sanghvi *et al.*, "Performance of an artificial intelligence algorithm for reporting urine cytopathology," *Cancer Cytopathology*, vol. 127, no. 10, pp. 658–666, 2019.
- [3] X. Zhang *et al.*, "Whole slide cervical cancer screening using graph attention network and supervised contrastive learning," in *Medical Image Computing and Computer Assisted Intervention–MICCAI 2022: 25th International Conference, Singapore, September 18–22, 2022, Proceedings, Part II*. Springer, 2022, pp. 202–211.
- [4] S. Cheng *et al.*, "Robust whole slide image analysis for cervical cancer screening using deep learning," *Nature communications*, vol. 12, no. 1, p. 5639, 2021.
- [5] L. Cao *et al.*, "A novel attention-guided convolutional network for the detection of abnormal cervical cells in cervical cancer screening," *Medical image analysis*, vol. 73, p. 102197, 2021.
- [6] H. Garud *et al.*, "High-magnification multi-views based classification of breast fine needle aspiration cytology cell samples using fusion of decisions from deep convolutional networks," in *Proceedings of the IEEE conference on computer vision and pattern recognition workshops*, 2017, pp. 76–81.
- [7] A. Teramoto *et al.*, "Automated classification of lung cancer types from cytological images using deep convolutional neural networks," *BioMed research international*, vol. 2017, 2017.
- [8] J. Li *et al.*, "Hybrid supervision learning for pathology whole slide image classification," in *Medical Image Computing and Computer Assisted Intervention–MICCAI 2021: 24th International Conference, Strasbourg, France, September 27–October 1, 2021, Proceedings, Part VIII*. Springer, 2021, pp. 309–318.
- [9] E. Davey *et al.*, "Effect of study design and quality on unsatisfactory rates, cytology classifications, and accuracy in liquid-based versus conventional cervical cytology: a systematic review," *The Lancet*, vol. 367, no. 9505, pp. 122–132, 2006.
- [10] T. Sun *et al.*, "Diagnostic value of a comprehensive, urothelial carcinoma-specific next-generation sequencing panel in urine cytology and bladder tumor specimens," *Cancer Cytopathology*, vol. 129, no. 7, pp. 537–547, 2021.
- [11] H. Jiang *et al.*, "Deep learning for computational cytology: A survey," *Medical Image Analysis*, p. 102691, 2022.
- [12] W. Morrison *et al.*, "Advantages and disadvantages of cytology and histopathology for the diagnosis of cancer," vol. 8, no. 4, 1993, pp. 222–227.
- [13] P. Dey *et al.*, *Basic and advanced laboratory techniques in histopathology and cytology*. Springer, 2018.
- [14] M. Plissiti *et al.*, "Automated detection of cell nuclei in pap stained cervical smear images using fuzzy clustering," in *4th European Conference of the International Federation for Medical and Biological Engineering: ECIFMBE 2008 23–27 November 2008 Antwerp, Belgium*. Springer, 2009, pp. 637–641.
- [15] T. Chankong *et al.*, "Automatic cervical cell segmentation and classification in pap smears," *Computer methods and programs in biomedicine*, vol. 113, no. 2, pp. 539–556, 2014.
- [16] N. Kurian *et al.*, "Deep multi-scale u-net architecture and label-noise robust training strategies for histopathological image segmentation," in *2022 IEEE 22nd International Conference on Bioinformatics and Bioengineering (BIBE)*. IEEE, 2022, pp. 91–96.
- [17] J. Yu *et al.*, "Local-to-global spatial learning for whole-slide image representation and classification," *Computerized Medical Imaging and Graphics*, p. 102230, 2023.
- [18] A. Saikia *et al.*, "Comparative assessment of cnn architectures for classification of breast fnac images," *Tissue and Cell*, vol. 57, pp. 8–14, 2019.
- [19] H. Zerouaoui *et al.*, "Classifying breast cytological images using deep learning architectures," in *HEALTHINF*, 2022, pp. 557–564.
- [20] H. Zerouaoui *et al.*, "Deep hybrid architectures for binary classification of medical breast cancer images," *Biomedical Signal Processing and Control*, vol. 71, p. 103226, 2022.
- [21] J. Deng *et al.*, "Imagenet: A large-scale hierarchical image database," in *2009 IEEE conference on computer vision and pattern recognition*. Ieee, 2009, pp. 248–255.
- [22] H. Chen *et al.*, "A variational approach for learning from positive and unlabeled data," *Advances in Neural Information Processing Systems*, vol. 33, pp. 14 844–14 854, 2020.
- [23] C. Chen *et al.*, "Crossvit: Cross-attention multi-scale vision transformer for image classification," in *Proceedings of the IEEE/CVF international conference on computer vision*, 2021, pp. 357–366.
- [24] P. Du *et al.*, "Analysis of learning from positive and unlabeled data," *Advances in neural information processing systems*, vol. 27, 2014.
- [25] M. Hou *et al.*, "Generative adversarial positive-unlabelled learning," *arXiv preprint arXiv:1711.08054*, 2017.
- [26] C. Zhang *et al.*, "Positive and unlabeled learning with label disambiguation," in *IJCAI*, 2019, pp. 4250–4256.
- [27] Z. Zhao *et al.*, "Positive-unlabeled learning for cell detection in histopathology images with incomplete annotations," in *Medical Image Computing and Computer Assisted Intervention–MICCAI 2021: 24th International Conference, Strasbourg, France, September 27–October 1, 2021, Proceedings, Part VIII*. Springer, 2021, pp. 509–518.
- [28] K. Yu *et al.*, "Anatomy-guided weakly-supervised abnormality localization in chest x-rays," in *Medical Image Computing and Computer Assisted Intervention–MICCAI 2022: 25th International Conference, Singapore, September 18–22, 2022, Proceedings, Part V*. Springer, 2022, pp. 658–668.
- [29] M. Zuluaga *et al.*, "Learning from only positive and unlabeled data to detect lesions in vascular ct images," in *Medical Image Computing and Computer-Assisted Intervention–MICCAI 2011: 14th International Conference, Toronto, Canada, September 18–22, 2011, Proceedings, Part III*. Springer, 2011, pp. 9–16.
- [30] R. Kiryo *et al.*, "Positive-unlabeled learning with non-negative risk estimator," *Advances in neural information processing systems*, vol. 30, 2017.
- [31] H. Zhang *et al.*, "mixup: Beyond empirical risk minimization," *arXiv preprint arXiv:1710.09412*, 2017.
- [32] J. Devlin *et al.*, "Bert: Pre-training of deep bidirectional transformers for language understanding," *arXiv preprint arXiv:1810.04805*, 2018.
- [33] D. Hendrycks *et al.*, "Gaussian error linear units (gelus)," *arXiv preprint arXiv:1606.08415*, 2016.
- [34] J. Ba *et al.*, "Layer normalization," *arXiv preprint arXiv:1607.06450*, 2016.
- [35] A. Dosovitskiy *et al.*, "An image is worth 16x16 words: Transformers for image recognition at scale," *arXiv preprint arXiv:2010.11929*, 2020.
- [36] K. He *et al.*, "Deep residual learning for image recognition," in *Proceedings of the IEEE conference on computer vision and pattern recognition*, 2016, pp. 770–778.
- [37] S. Nojima *et al.*, "A deep learning system to diagnose the malignant potential of urothelial carcinoma cells in cytology specimens," *Cancer Cytopathology*, vol. 129, no. 12, pp. 984–995, 2021.
- [38] G. Campanella *et al.*, "Clinical-grade computational pathology using weakly supervised deep learning on whole slide images," *Nature medicine*, vol. 25, no. 8, pp. 1301–1309, 2019.
- [39] M. Schlichtkrull *et al.*, "Modeling relational data with graph convolutional networks," in *The Semantic Web: 15th International Conference, ESWC 2018, Heraklion, Crete, Greece, June 3–7, 2018, Proceedings 15*. Springer, 2018, pp. 593–607.
- [40] S. Yu *et al.*, "Multi-scale enhanced graph convolutional network for early mild cognitive impairment detection," in *Medical Image Computing and Computer Assisted Intervention–MICCAI 2020: 23rd International Conference, Lima, Peru, October 4–8, 2020, Proceedings, Part VII*. Springer, 2020, pp. 228–237.
- [41] T. Chen *et al.*, "A simple framework for contrastive learning of visual representations," in *International conference on machine learning*. PMLR, 2020, pp. 1597–1607.
- [42] X. Chen *et al.*, "Improved baselines with momentum contrastive learning," *arXiv preprint arXiv:2003.04297*, 2020.
- [43] Y. Xu *et al.*, "Multi-positive and unlabeled learning," in *IJCAI*, 2017, pp. 3182–3188.
- [44] G. Blanchard *et al.*, "Semi-supervised novelty detection," *The Journal of Machine Learning Research*, vol. 11, pp. 2973–3009, 2010.